Multi-arm and Substituent Effects on Charge Transport of Organic Hole Transport Materials

Kun-Han Lin,[‡] Antonio Prlj,[‡] Liang Yao,[§] Nikita Drigo,[¶] Han-Hee Cho,[§] Mohammad Khaja Nazeeruddin,[¶] Kevin Sivula[§] and Clémence Corminboeuf[‡*]

[‡]Laboratory for Computational Molecular Design, Institute of Chemical Sciences and Engineering, Ecole Polytechnique Fédérale de Lausanne (EPFL), CH-1015 Lausanne, Switzerland.

§Molecular Engineering of Optoelectronic Nanomaterials Lab, Institute of Chemical Sciences and Engineering, Ecole Polytechnique Fédérale de Lausanne (EPFL), CH-1015 Lausanne, Switzerland.

¶Group for Molecular Engineering of Functional Materials, Institute of Chemical Sciences and Engineering, Ecole Polytechnique Fédérale de Lausanne (EPFL Valais), CH-1951 Sion, Switzerland

ABSTRACT: We explore several potential dopant-free triphenylamine-based HTMs for perovskite solar cells by combining two design strategies: (1) the incorporation of multi-arm for mobility enhancement and (2) including Lewis bases that assist in defect passivation. Through multi-scale computations along with the analysis of electronic structure, molecular transport network and data clustering, we established the relationship between hole mobility, transport parameters, intrinsic molecular properties and molecular packing. Our results showed that multi-arm design can be an effective strategy for four-fold hole mobility enhancement (from 7×10^{-6} to 3×10^{-5} $cm^2V^{-1}s^{-1}$) through reducing the reorganization energy and energetic disorder. Furthermore, ionization potential (IP) optimization by changing substituents was performed since the IP decreases with increasing number of arms. By adequate choice of substituents, the IP approaches the minus valence band maximum of $MAPbI_3$ and the hole mobility is further increased by ~3 times. The simulated mobility is in fair agreement with the one obtained from field-effect transistors, supporting our computational protocols.

1. Introduction

Organic–inorganic hybrid perovskite solar cells (PSCs) are considered as one of the most promising candidates to meet the increasing energy demand. Since their emergence in 2009, their power conversion efficiency (PCE) has increased from 3.8% to more than 22%.[1,2] To further improve PCE, it is essential to identify the ideal material for each device component. The most important layer in the PSC device is the active perovskite, which is responsible for absorbing sunlight and generating free charge carriers. In addition to the main active perovskite, the hole transport (selective) layers play a crucial role in reducing interfacial electron-hole recombination and serve as a protective coating that retards moisture.[3–6] As a result, considerable effort has been directed toward discovering promising hole transport materials (HTMs), especially small organic molecule-based HTMs.[7–13]

The desired HTMs properties in perovskite solar cell are well-defined: (a) a suitable ionization potential (IP) and (b) a high hole mobility (μ). A suitable ionization potential (IP) facilitates hole injection and maximizes the open circuit voltage (V_{oc}), while a high hole mobility (μ) affords efficient hole transport from the perovskite layer to the electrode, leading to a high fill factor (FF).[14–16] In addition, HTMs with high μ can serve as dopant-free HTMs, avoiding introducing deliquescent salts such as Li-TFSI which is detrimental to long-term stability. Despite recent effort in the field,[17–26] the current understanding of the "chemical structure"-property (*i.e.*, hole mobility) relationship for amorphous HTMs is still murky. This lack of knowledge hampers the discovery pace of promising HTMs and, for this reason, systematic investigations of the influence of molecular structure on the hole mobility are beneficial.[15,27] Correspondingly, computer simulations undertaken at the molecular level are powerful tools in revealing this non-trivial relationship, as demonstrated by Andrienko and Wetzelaer *et. al.*,[28] who compared the hole transport parameters and mobility of five common organic amorphous semiconductors with those obtained by experiments.

Because of the limited understanding of the structure-mobility relationship, current searches for new HTMs tend to rely on trial-and-error approaches. For example, Son *et al.*[8] and Dai *et al.*[22] considered the effect of the number of triphenylamine (TPA) moieties attached to the central core on PSC performance, finding that the HTM hole mobility increases with the number of TPA arms. Another relevant example involved increasing the PCE by introducing more Lewis bases, from zero (TPAC0M) to three methoxy groups (TPAC3M) in order to reduce electron-hole recombination.[29] Thus, a legitimate question is can these two strategies be combined with one another? Assuming we retain the ability of defect passivation by controlling the number of -MeO, can hole mobility be enhanced by introducing additional arms? How do these molecular modifications alter the IP? Starting from TPAC3M (referred to as TPA1C3M later),

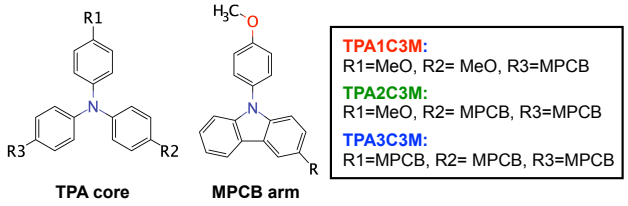

Figure 1. The molecular structure of the TPA core, the MPCB arm, the MeO group, as well as the TPA1C3M, TPA2C3M and TPA3C3M molecules.

which is already a promising dopant-free HTM leading to a PSC with ~16% PCE,[29] here, we consider derivatives with increasing numbers of 9-(4-methoxyphenyl)carbazole arms (MPCB arms, as shown in **Figure 1**), which are investigated through a multi-scale computational protocol. The relationship between the most critical charge transport parameters and the properties are investigated using electronic structure computations, molecular transport network and dimer-configuration clustering. Our results demonstrate that hole mobility increases with the number of MPCB arms attached to the TPA core. However, introducing more arms leads to an unfavorable decrease in IP, which can be adjusted through careful chemical modification. The simulations of two of the best performing HTMs are compared with field-effect transistor measurements, showing good agreement between experimental and simulated hole mobilities. This finding highlights the relevance of our strategy that has the potential for applications stretching beyond the field of perovskite solar cells.

2. Results and discussion

Multi-arm effect on charge transport properties

Hole mobility is obtained from kinetic Monte Carlo (kMC) simulations, for which the input is the hole hopping rates calculated for each molecular pair *ij* (molecular dimer) using non-adiabatic semi-classical Marcus charge transfer theory.[30] Each of the charge transport parameters given in the computational details (*e.g.*, reorganization energy λ, transfer integrals J_{ij} and site energy difference ΔE_{ij} in **Equation 4**) are discussed below.

The Reorganization energy, (computed with the 4-point method) decreases from 213 meV to 156 meV while increasing the number of MPCB arms (**Figure 2(a)**). Since low reorganization energies lead to high charge transfer rates, increasing the number of MPCB arms attached to the TPA core is an effective strategy that might underpin the outstanding performance of existing multi-arm HTMs.[22,31,32] At room temperature, the charge transfer rate of TPA3C3M is two times that of TPA1C3M, assuming a zero site-energy difference ($\Delta E_{ij} = 0$) and the same transfer integrals (as shown in **Equation 1**).

$$\frac{\omega_{TPA3C3M}}{\omega_{TPA1C3M}} = \sqrt{\frac{\lambda_{TPA1C3M}}{\lambda_{TPA3C3M}}} \exp\left[-\frac{\lambda_{TPA3C3M}-\lambda_{TPA1C3M}}{4k_BT}\right] \approx 2.03 \qquad (1)$$

The reason for the significant decrease in λ is extended conjugation, as visualized (**Figure S1**) by the HOMO becoming more spatially delocalized through the MPCB arms when moving from TPA1C3M to TPA3C3M. Thus, it is not surprising that the trend in reorganization energy has been noted for similar molecules such as oligoacene, thienoacenes and oligothiophenes.[33,34]

The origin of the decreasing λ can be further investigated by a partitioning into each contributing vibrational mode using normal model analysis (NM). The reorganization energy determined through this method is 218 meV, 173 meV and 162 meV for TPA1C3M, TPA2C3M and TPA3C3M, respectively. The good agreement between λ obtained from NM and 4-point method indicates the anharmonic effect is insignificant in our case. Since the behavior and sums of the vibrational mode contributions for all three molecules are similar for λ_1 and λ_2 (see computational details, **Figure 3** and **Table S1**), the following discussion focuses only on λ_1. The key contributing normal modes are nearly the same for each of the three molecules (see arrows in **Figure 3** and the corresponding vibrational modes in **Figure S3-S5**). Interestingly, with the exception of the first band, TPA1C3M is always characterized by the largest contributions. Given that the relevant frequencies are the same for all molecules, the larger λ_1 contribution of TPA1C3M arises from a larger displacement (ΔQ_i^2, as shown in **Figure S3 to S5**). Overall, introducing more arms does not alter the major vibrational modes that contribute to the local electron-phonon coupling, but rather reduce the reorganization energy by attenuating the geometrical response between the charged and neutral state (*i.e.*, ΔQ_i^2 of these modes).

Energetic disorder: In organic amorphous materials, the lack of translational symmetry leads to a Gaussian or exponential distribution of the site energies, where the molecules with a site energy centered at the tail of the density of states serve as potential charge traps that hamper charge transport.[35] The dependence of charge mobility on the energetic disorder is described by a lattice model:[36,37]

$$\mu \propto \exp\left[-(C\beta\sigma)^2\right] \qquad (2)$$

where C is a coefficient that depends upon the model used and β is the inverse of temperature ($1/k_BT$). The exponential dependence emphasizes the crucial role of σ. The physical

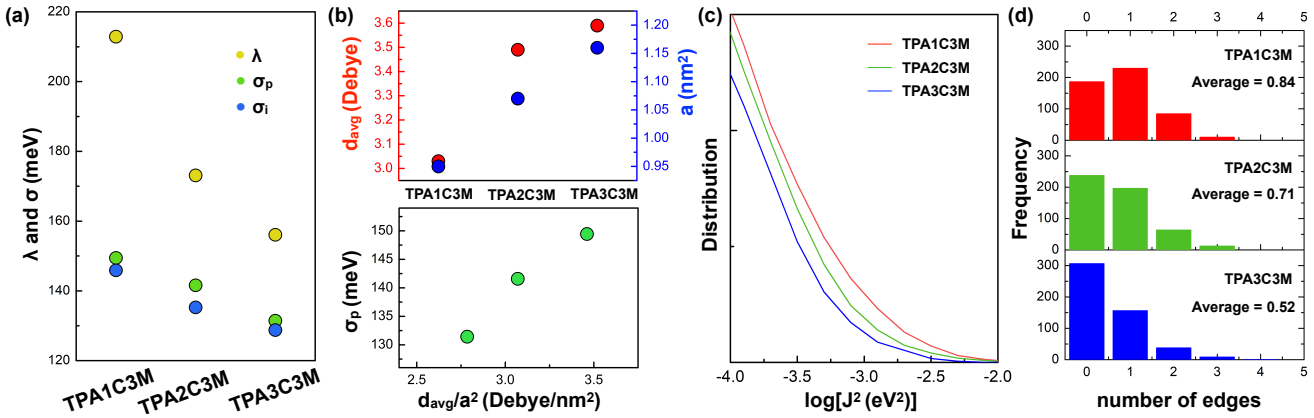

Figure 2. (a) Reorganization energy (λ, computed using 4-point method at B3LYP/6-31G(d,p) level), energetic disorder (electrostatic and polarization component, σ_p) and intrinsic energetic disorder (σ_i), (b1) average molecular dipole moment d_{avg} and lattice parameter a, (b2) a $\sigma_p - \frac{d_{avg}}{a^2}$ plot, (c) the overall transfer integral square distribution and (d) the histogram of number of edges for each hopping site with a threshold of 10^{-4} eV^2 for TPA1C3M, TPA2C3M and TPA3C3M molecules.

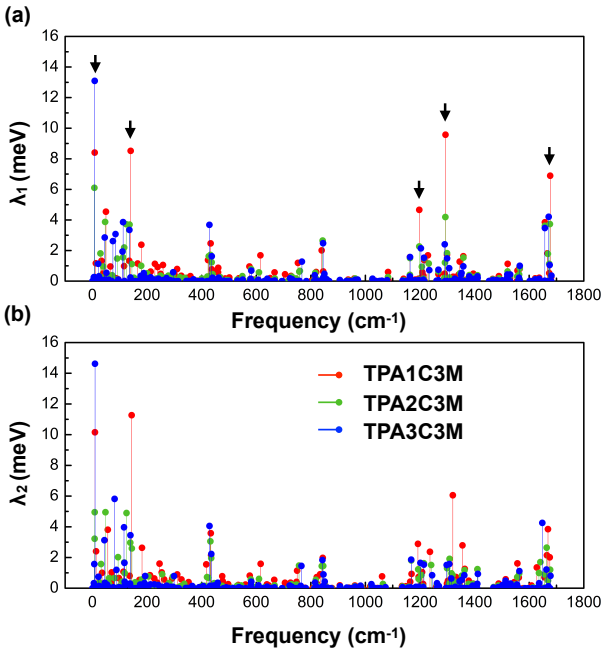

Figure 3. Frequency dependence reorganization energy computed using NM method B3LYP/6-31G(d,p) level for (a) neutral (λ_1) and (b) cationic (λ_2) geometry upon hole transfer process for TPA1C3M, TPA2C3M and TPA3C3M. The black arrows indicate the frequencies that make major contribution to reorganization energy.

origin of the energetic disorder can be understood from the partitioning:[38]

$$\sigma_{tot}^2 = \sigma_p^2 + \sigma_i^2 \quad (3)$$

were σ_{tot} is the total energetic disorder, σ_p the electrostatic and induction component and σ_i is the intrinsic component. σ_i arises from the molecular conformational disorder present in disordered organic materials, which leads to HOMO variation. On the other hand, σ_p results from the electrostatic interactions and the induction between a molecule (site) and its surrounding environment.

As shown in **Figure 2(a)**, σ_p decreases with an increase in the number of MPCB arms, from 149 meV to 131 meV. This can be explained by the correlated Gaussian disorder model (CGDM), which describes the energetic disorder using a dipole glass model (simple cubic lattice, for which the sites are occupied by randomly oriented dipoles).[39] The origin of σ in this model is purely electrostatic, with σ being proportional to the molecular dipole moment (d) and the inverse of the square of the cubic lattice parameter ($\frac{1}{a^2}$). We compute the average molecular dipole moment d_{avg} and effective lattice parameter a for each compound (see page 11 in the supporting information). Although both d_{avg} and a increase by a similar percentage (~20%) when going from 1 to 3 arms, the inverse square dependence of σ on a leads to an overall decrease in $\frac{d_{avg}}{a^2}$ (**Figure 2(b)**). The good correlation between σ_p and $\frac{d_{avg}}{a^2}$ indicates that the multi-arm design strategy can successfully reduce σ_p if the increase in molecular dipole moment is not significant compared to the increase in molecular size.

Similar to σ_p, the intrinsic energetic disorder also decreases from 146 meV to 129 meV when increasing the number of MPCB arms from one to three. Previous work by Wenzel *et al.* showed that σ_i correlates rather well with the variation in HOMO energy with respect to the easily-rotatable dihedral angles.[38] Similar correlations are observed between the HOMO of the molecule considered here and the dihedral angle between the carbazole group in MPCB and the benzene in the TPA core (**Figure S7**). The HOMO variation decreases with an increase in the number of arms, akin to the σ_i. trend. Since both σ_p and σ_i follow the same trend, the total energetic disorder follows the order TPA1C3M > TPA2C3M > TPA3C3M.

Transfer integrals also exhibit a broad distribution in disordered organic materials. As shown in **Figure 2(c)**, the population in the high transfer integral region [10^{-4}~10^{-2} eV^2] follows the trend TPA1C3M > TPA2C3M > TPA3C3M, suggesting that there are more molecular dimers with high transfer integrals in TPA1C3M than in its multi-armed counterpart. Apart from the magnitude of the transfer integrals, the connectivity of the molecular transport network is also crucial for rationalizing charge mobility.[40,41] We examined the transport network using two measures: (1) the average number of edges per site (E_{avg}) and (2) the Kirchoff transport index (K, see computational details).[42]

For a threshold value of 10^{-4} eV^2, the majority of the number of edges per site is either 0 or 1 for all three molecules. Going from TPA1C3M to TPA3C3M, the frequency of 1 and 2 edges gradually decreases while that of 0 edges increases. Overall, the average number of edges per hopping site decreases as the number of MPCB arms increases, from 0.84 to 0.52. Similar trends are observed for threshold values of 10^{-5} and 10^{-6} eV^2 (**Figure S8** and **Table S3**). The Kirchoff transport index (**Table S3**) correlates well with E_{avg}, suggesting better transport network properties for TPA1C3M.

In short, TPA1C3M outperforms its counterparts in terms of both the overall distribution and the spatial connectivity of the transfer integrals. Generally, two factors determine the magnitude of the transfer integrals for hole transfer: (1) the

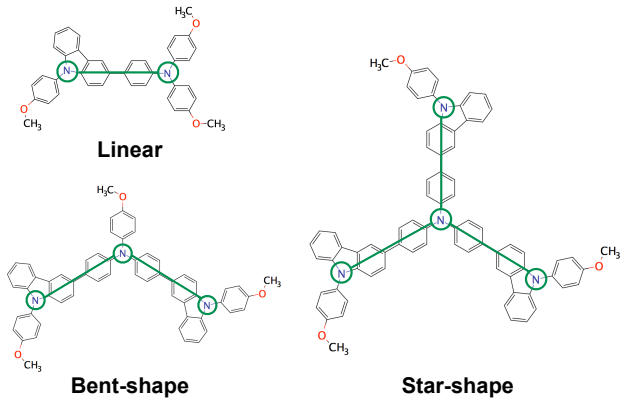

Figure 4. The molecular shape of TPA1C3M, TPA2C3M and TPA3C3M molecules.

intrinsic molecular property (HOMO) and (2) the molecular packing (dimer geometry).[34] Here,, the molecular shape varies from linear (TPA1C3M), to bent (TPA2C3M) to star shape

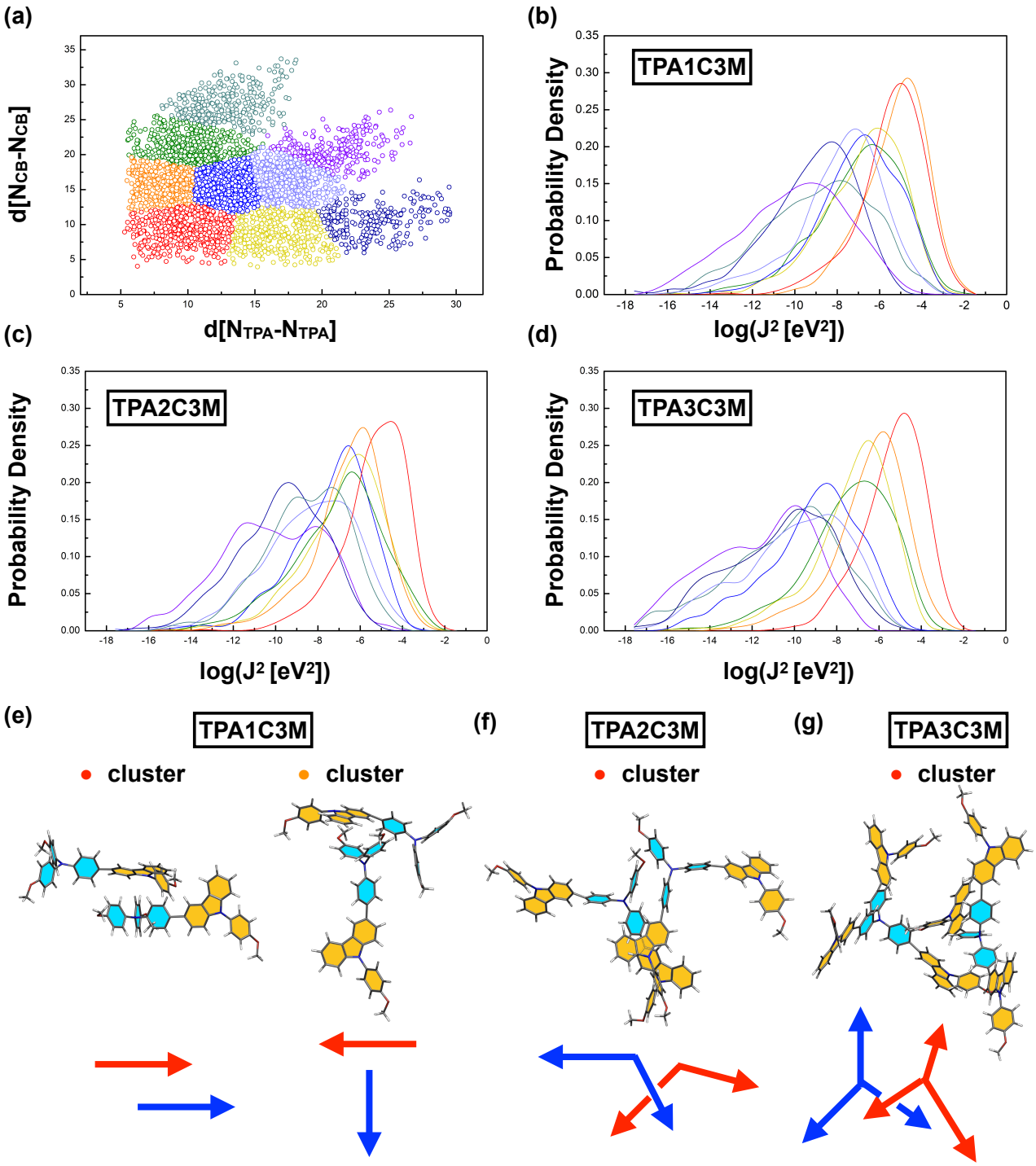

Figure 5. (a) Clustering of a 2D configurational space for TPA1C3M into 9 clusters (specified by color), each dot represents a molecular dimer. The d[N_{TPA}-N_{TPA}] stands for the distance between two nitrogen atoms on TPA cores of two molecules and the d[N_{CB}-N_{CB}] represents the distance between two nitrogen atoms on carbazole (CB) arms; the probability density of transfer integral square for the corresponding cluster (with the same color) for (b) TPA1C3M, (c) TPA2C3M and (d) TPA3C3M; the prototypical dimer configuration (centroid of each cluster) for (e) TPA1C3M, (f) TPA2C3M and (g) TPA3C3M. The arrow is a sketch for the prototypical dimer configurations, pointing from nitrogen atom of TPA core (light blue) to that of MPCB arms (light orange).

(TPA3C3M), which naturally results in very different molecular packing (dimer configurations) (**Figure 4** and **Figure 5**). Insightful information can be extracted from the relationship between the molecular packing and the transfer integrals for each amorphous organic material even though the intrinsic change in HOMO also comes into play. The relations are analyzed via data clustering in an N-dimensional space where N is the number of geometrical descriptors used to describe the representative dimer configurations for each molecule (see computational details and SI).

The TPA1C3M dimer configurations can be represented by points with coordinates (d[N_{TPA}-N_{TPA}], d[N_{CB}-N_{CB}]) in a 2-

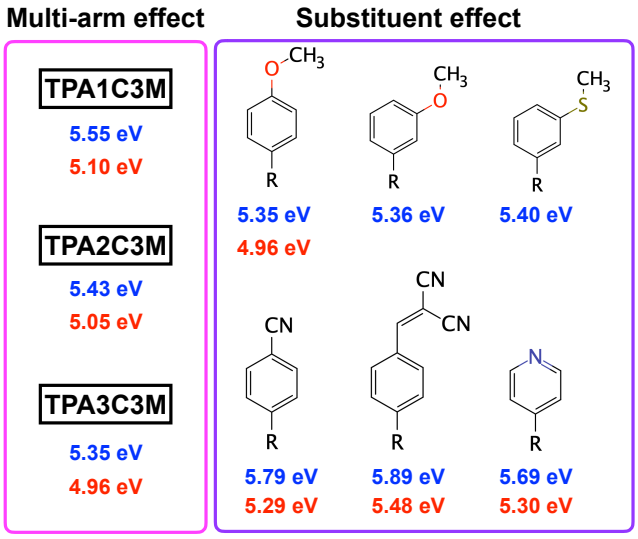

Figure 6. Ionization potential of TPA1C3M, TPA2C3M, TPA3C3M and the derivatives of TPA3C3M in isolated gas state (IP_{iso}, blue) and with solid-state correction (IP_{solid}, red).

dimensional (2D) configurational space, as shown in **Figure 5(a)**. We plotted the probability density of the square of the transfer integral for each cluster on the 2D configurational space (**Figure 5(b)**). Clusters located at the bottom left of **Figure 5(a)**, represent close-contact dimer configurations, possess distributions with peaks positioned at higher J^2 region compared to their top right counterparts. Among all the clusters, two (red and orange) possess a J^2 distribution with a peak at $10^{-5} \sim 10^{-4}$ eV^2, which make major contributions to the overall J^2 distribution in the high transfer integral region (**Figure 2(c)**). The prototypical dimer configurations of these two clusters, which are characterized by "parallel" and "T-shape" arrangements, are shown in **Figure 5(e)** (for other clusters, see **Figure S11 to S13**). It is not surprising that these two types of molecular packing lead to high transfer integrals. Furthermore, the prototypical dimer configurations for the orange and yellow clusters, which are roughly symmetric with respect to the diagonal of 2D configurational space, are both "T-shaped" and differ that the moieties involved at the branch point of "T" are different (TPA group for orange cluster and MPCB group for yellow cluster). This results in a difference in the degree of π-π overlap, where the former has two phenyl groups in close contact with the other molecule at the branch point, while the latter has only one, which leads to a left-shifted peak in J^2 distribution for the yellow cluster.

Using the same treatment for TPA2C3M/TPA3C3M as for TPA1C3M, the probability density of transfer integral square for each cluster is shown in **Figure 5(c)** and **(d)**. Unlike TPA1C3M, only one cluster (red) possess a J^2 distribution with a peak at $10^{-5} \sim 10^{-4}$ eV^2, with the corresponding characteristic dimer configurations being shown in **Figure 4(f)** and **(g)**. In the region of $10^{-6} \sim 10^{-5}$ eV^2, TPA2C3M possesses two clusters (orange and yellow) with peaks located in this range, while TPA3C3M only has one cluster (orange) in the same region. Since the number of dimer configurations for each cluster is quite similar, the difference in J^2 probability distribution explains the observed trend in the distribution in the high J^2 region: TPA1C3M > TPA2C3M > TPA3C3M (**Figure 2(c)**).

Hole mobility: To sum up, the reorganization energy, total energetic disorder and transfer integrals all decrease when the number of MPCB arms is increased. Reducing the first two parameters favors high hole mobility, while decreasing the last has the opposite effect. Overall, the simulated hole mobility of TPA1C3M, TPA2C3M and TPA3C3M are 7.34×10^{-6}, 1.49×10^{-5} and 3.09×10^{-5} $cm^2V^{-1}s^{-1}$, respectively (**Figure 8**) indicating that the gain from lowering the reorganization energy and energetic disorder surpasses the loss from the lower transfer integrals when more MPCB arms are introduced. This 4.2 fold enhancement in hole mobility proves that the multi-arm design strategy is effective for this molecule. Although the totality of multi-arm design principles should be examined for other molecules, the computational protocol and the analysis adopted here is broadly applicable to future systematic investigations.

Optimization of the ionization potential

The computed ionization potentials of HTMs in isolated gas phase (IP_{iso}) and with solid state correction (IP_{solid}) are shown in **Figure 6**. Although the hole mobility is augmented by the number of MPCB arms, the IP_{solid} decreases from 5.10 eV to 4.96 eV, which is unfavorable to the V_{oc}. Thus, it would be beneficial to adjust the IP via chemical modification while preserving (or even improving) the hole mobility. The strategy is to alter the molecular structure of TPA3C3M minimally, conserving the defect passivation ability (*e.g.*, the number of Lewis bases) by replacing the methoxyphenyl groups located on the MPCB arms with stronger electron-withdrawing groups or alternative substitution site. Since IP_{iso} and IP_{solid} show similar trends, we use the cost-effective IP_{iso} as a preliminary screening criterion, followed by IP_{solid} computations for the potential HTMs.

Seok *et al.* showed that by displacing half of the methoxy groups on Spiro-OMeTAD from the para (electron-donating) to the meta ((electron-withdrawing) position increased the IP by ~0.1 eV.[25] In our case, this modification only raises the IP_{iso} from 5.35 eV to 5.36 eV. Further enhancement can be achieved through heteroatom substitution and replacing m-MeO with m-MeS groups,[43] leading to an IP of 5.40 eV. Given that these two strategies are not sufficient, we introduced stronger electron-withdrawing groups (*e.g.*, benzonitrile, benzylidenemalononitrile and pyridine) that are traditionally used for tuning the IP of HTMs (**Figure 6**).[44–46] The IP_{iso} effectively increases from 5.35 eV (methoxyphenyl) to 5.79 eV (benzonitrile; TPA3C3CN), 5.89 eV (benzylidenemalononitrile; TPA3C6CN) and 5.69 eV (pyridine; TPA3C3PD). Further examination shows that their IP_{solid}, 5.29 eV, 5.48 eV and 5.30 eV, approach the value of the minus valance band maximum of $MAPbI_3$.[16]

Substituent effect on charge transport properties

Analogous to the previous sections, we now discuss substituent effects from TPA3C3M to TPA3C3CN, TPA3C6CN and TPA3C3PD, on each transport parameters: λ, σ and J_{ij}.

Reorganization energy: The reorganization energy (using the 4-point method, see **Table S2** for the NM results) marginally increases from 156 meV to 168 meV (TPA3C3CN), 181 meV (TPA3C6CN) and 168 meV (TPA3C3CN) (**Figure 7(a)**) when stronger electron-withdrawing substituents are introduced. Overall, this effect is less significant than varying the number of arms (25 meV vs 57 meV from TPA1C3M to TPA3C3M). A crude estimation using **Equation 1** suggests that the influence of the reorganization energy change on charge transport by

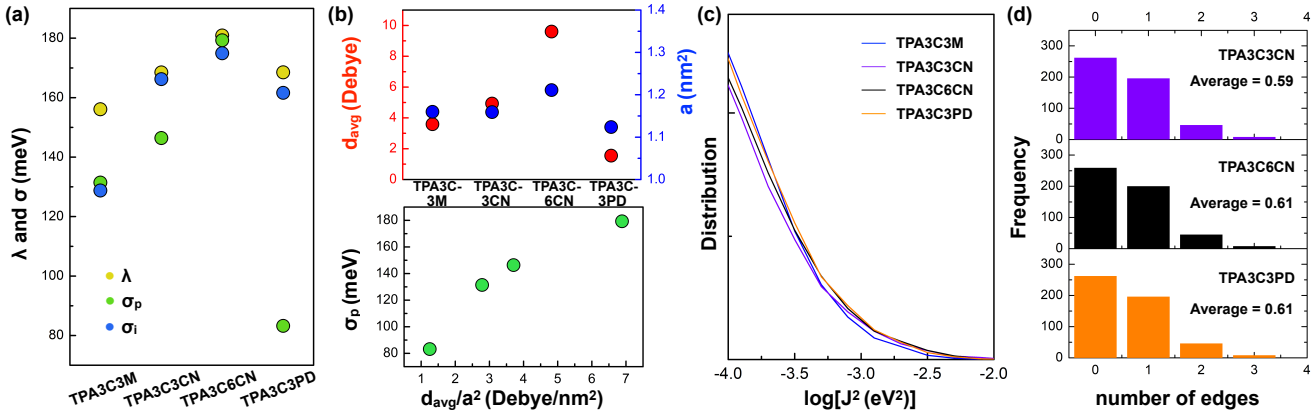

Figure 7. (a) Reorganization energy (λ, computed using 4-point method at B3LYP/6-31G(d,p) level), energetic disorder (electrostatic and polarization component, σ_p) and intrinsic energetic disorder (σ_i), (b1) average molecular dipole moment d_{avg} and lattice parameter a, (b2) a $\sigma_p - \frac{d_{avg}}{a^2}$ plot, (c) the overall transfer integral square distribution and (d) the histogram of number of edges for each hopping site with a threshold of 10^{-4} eV^2 for TPA1C3M, TPA2C3M and TPA3C3M molecules.

introducing different substituents is minor, with a transfer rate 0.73/0.86 times that of TPA3C3M for TPA3C6CN/TPA3C3CN.

Energetic disorder: σ_p (**Figure 7(a)**) increases from 131 meV to 146 meV (TPA3C3CN) and 179 meV (TPA3C6CN). Yet, replacing the methoxyphenyl by pyridine groups strongly reduces σ_p (by 51 meV). This contrast essentially originates from the molecular dipole moment, as shown in **Figure 7(b)**. Introducing benzylidenemalononitrile groups raises the average molecular dipole moment from 3.59 to 9.60 Debye. The intrinsic energetic disorder follows a similar trend, with the exception of the σ_i of TPA3C3PD, which is larger than that of TPA3C3M. The total energetic disorder evolves as: TPA3C6CN > TPA3C3CN > TPA3C3M > TPA3C3PD.

Transfer integrals: All systems exhibit a similar square of the transfer integral distribution in the region where the transfer integral is highest [10^{-4}~10^{-2} eV^2] (**Figure 7(c)**), indicating that both the variations in the HOMO (**Figure S2**) and changes in molecular packing are only slightly affected by the substituent. This is confirmed from the average connectivity plot of the three molecules examined in **Figure 7(d)** (very similar and slightly better than that of TPA3C3M), the Kirchoff transport index (**Table S3**) and the clustering analysis (**Figure S14),** which each show that substituent modification leads to a similar molecular packing and better molecular transport network.

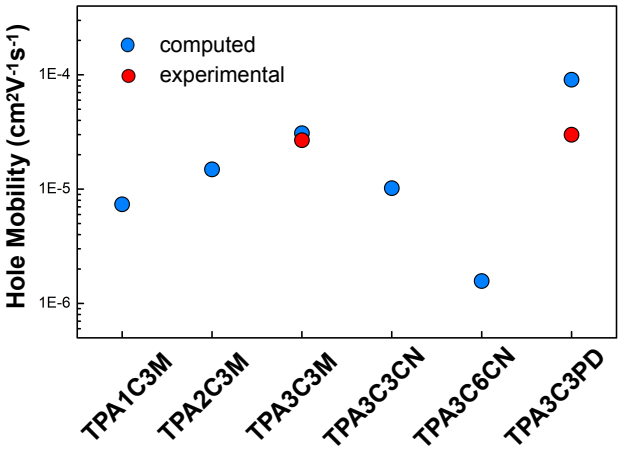

Figure 8. The computed and experimentally measured hole mobility (average result from four transistors) for all molecules.

Hole mobility: The hole mobility of TPA3C3CN, TPA3C6CN and TPA3C3PD is predominantly determined by the reorganization energy and the total energetic disorder (1.02×10^{-5}, 1.57×10^{-6} and 9.07×10^{-5} cm^{2}V^{-1}s^{-1}, respectively, **Figure 8**). Modifying the substituents from TPA3C3M to TPA3C6CN decreases hole mobility by more than an order of magnitude, whereas TPA3CPD is increased by ~3 times. On the basis of the previous evaluation of the reorganization energy contribution, we can conclude that the energetic disorder, (especially σ_p) is the main source for the variation in hole mobility. This highlights the crucial role of the molecular dipole moment as a design principle. To verify our simulated results, we measured the hole mobility of TPA3C3M and TPA3C3PD, showing highest simulated hole mobility, using bottom contact bottom gate field effect transistors (FETs) prepared by solution processing (**Figure 8**). Our predictions are in fair agreement with the experimental mobility of TPA3C3M. The larger computed TPA3C3PD mobility may arise from the hole concentration effect: the FET mobility is extracted at high charge-carrier concentration, while the simulations are performed with a single charge carrier. The trap filling effect at high carrier concentration makes the hole mobility less sensitive to the energetic disorder, which is the parameter most responsible for the difference in the simulated hole mobility of TPA3C3M and TPA3C3PD. For devices operating at lower hole concentrations (*e.g.*, perovskite solar cell), we expect better charge transport for TPA3C3PD than for TPA3C3M.

3. Summary

In summary, we investigated multi-arm and substituent effects in TPA-based HTMs using multi-scale simulations involving density functional theory computations, classical forcefield molecular dynamics, and kMC simulations. The effect of molecular modifications on crucial transport parameters, the reorganization energy, the energetic disorder and the transfer integrals were evaluated through electronic structure analysis,

graph theory and data clustering. The reorganization energy, the energetic disorder and the transfer integrals all decrease when the number of MPCB arms is increased. Yet, the effect of reorganization energy and energetic disorder dominate the transfer integrals, which leads to an overall enhancement of the hole mobility. Despite the effectiveness of the multi-arm design strategy on hole transport, the IP decreases when the number of arms is increased, which is unfavorable in terms of V_{oc}. Further optimization of the IP was then undertaken in order to retain the high mobility of TPA3C3M while maintaining the original molecular structure as much as possible to minimize changes in molecular packing. Specifically, modification of the substituents attached to carbazole arms can be used to tune the IP where values can approach the minus valance band maximum of $MAPbI_3$. However, it should be noted that this design strategy may, at the same time, result in HTMs with large molecular dipole moments (TPA3C3CN, TPA3C6CN), which may lead to significant energetic disorder and lower hole mobility. A clever choice of substituents that yields a reduced molecular dipole moment and an enhancement of mobility is TPA3C3PD. From a practical point of view, TPA3C3PD and TPA3C3CN proposed in this work are better than our initial prototypical molecule, TPA1C3M, in terms of both IP and hole mobility. Our results show that promising HTMs can be achieved by modifying each transport parameters through multi-arm and substituent optimization, which can be adopted for the future design of HTMs or amorphous organic semiconductors. The simulated results show reasonable agreement with the mobility measured using FET devices for two HTMs with the highest hole mobility, which supports our computational protocols.

From a general viewpoint, the multi-arm effect influences all transport parameters at the same time, where the hole mobility is a subtle interplay between these parameters. Hence, the universality of this design strategy should be further examined. However, the transfer integrals and effective lattice parameter, the multi-molecule properties, can remain nearly unchanged through minimally modifying the molecular structures. Modifying substituents thus serves as an effective and efficient strategy to further enhance the hole mobility via minimizing the molecular dipole moment (a single-molecule property). We believe that both our computational protocols and our analysis highlighted here will be useful for future work aimed at investigating the structure-mobility relationship of amorphous organic semiconductors.

4. Methodology

4.1 Computational Details

Model for amorphous morphology

The amorphous morphology was generated starting from a unit cell with 64 randomly-placed molecules using Packmol. The system was minimized using the conjugate gradient algorithm and then equilibrated in the NPT ensemble (700K, 1bar) by performing classical molecular dynamics (MD) simulation. The equilibrated system was then extended into a 2x2x2 supercell with 512 molecules followed by equilibration (700K, 1bar) for 5 ns. Equilibration in the (300K, 1bar) NPT ensemble was then performed until the density reached equilibrium (~50 ns). A final 10-ns production run generated 1000 structures (snapshots) used in the kinetic Monte Carlo simulations.

The MD simulations were performed under periodic boundary condition with the Gromacs package[47,48,49] and CGenFF[50,51] force field along with charge obtained by restrained electrostatic potential (RESP)[52] procedure based on HF/6-31G**. The temperature and pressure control were using velocity rescaling with a stochastic term[53] (τ_T = 1.0 ps) and an isotropic coupling for the pressure from a Berendsen barostat (P_0 = 1 bar, $\chi = 4.5 \times 10^{-5}$ bar^{-1}, τ_P = 1.0 ps). The time step used in all simulations was 1 fs and bonds involving H atoms were constrained using the Linear Constraint Solver (LINCS) algorithm. A cutoff of 12 Å was applied to the van der Waals interaction through force-switch mode. As for electrostatic interactions, the particle mesh Ewald (PME) method was employed with a 0.12 nm Fourier spacing.

Charge transport simulations

For amorphous organic materials, the charge transport is well described by the hopping model, where a charge (electron/hole) is assumed to be instantaneously localized on one molecule (or a hopping site). The charge hopping rate between molecules can be evaluated using non-adiabatic semi-classical Marcus charge transfer theory:[30]

$$\omega_{ij} = \frac{J_{ij}^2}{\hbar}\sqrt{\frac{\pi}{\lambda k_B T}}\exp\left[-\frac{(\Delta E_{ij}-\lambda)^2}{4\lambda k_B T}\right] \quad (4)$$

where T is the temperature, J_{ij} is the transfer integral (sometimes referred to as electronic coupling) between the i and j sites, ΔE_{ij} is the site energy difference $E_i - E_j$ and λ is the reorganization energy. From the equation above, it is clear that high transfer integral and low reorganization energy lead to a high hopping rate between two sites, which, in turn, leads to high charge mobility. In addition to J_{ij} and λ, the spread of the site energy in an amorphous material is crucial.

The reorganization energy associated with the hole transfer process is related to the local electron-phonon coupling, which can be evaluated in two ways.[54,55] The first is the adiabatic potential energy surface method (the 4-point method), where reorganization energy is expressed as:

$$\lambda = \lambda_1 + \lambda_2 = (E_{\mathrm{nC}} - E_{\mathrm{nN}}) + (E_{\mathrm{cN}} - E_{\mathrm{cC}}) \quad (5)$$

where E_{nN} (E_{cC}) is the total energy of the neutral (cationic) molecule in neutral (cationic) geometry and E_{nC} (E_{cN}) is the energy of the neutral (cationic) molecule in cationic (neutral) geometry. The second method is the normal-mode (NM) analysis, which partitions the total reorganization energy into contribution from each vibrational mode. As such, the reorganization energy is expressed as:

$$\lambda = \lambda_1 + \lambda_2 = \sum_i \lambda_{1_i} + \sum_j \lambda_{2_j} = \sum_i \frac{1}{2}\omega_i \Delta Q_i^2 + \sum_j \frac{1}{2}\omega_j \Delta Q_j^2 \quad (6)$$

where $\lambda_{1_i}/\lambda_{2_j}$ is the contribution to reorganization energy from the vibrational mode i/j of the neutral/cationic geometry, ω_i/ω_j is the vibrational frequency of the mode i/j and $\Delta Q_i/\Delta Q_j$ represents the displacement along the i^{th}/j^{th} mode coordinate between the equilibrium positions of neutral and cationic states. We compute the reorganization energy using the two methods at the B3LYP[56,57]/6-31G(d,p) level with D3BJ[58] correction and Gaussian16 software[59]. The NM analysis was performed using DUSHIN and Gaussian16 in tandem.

Site energies are computed using the Thole model, where the correction terms resulting from the electrostatic and polarization effects from the environment (surrounding molecules and external electric field) are added to the HOMO of an isolated gas molecule.[60–63] The partial charges needed in

this model for the neutral and cationic states were generated via CHelpG.[64] We extract the energetic disorder present in HTMs using the Gaussian disorder model, where the energetic disorder (σ) is obtained from fitting the histogram of energy difference (ΔE_{ij}) to the Gaussian distribution.[61,65]

In order to efficiently compute the transfer integral of every molecular pair *ij* in the neighbor list, we adopted ZINDO-based Molecular Orbital Overlapping (MOO) method.[66,67] The results obtained from this method have been shown to be in reasonable agreement with those computed at the B3LYP/6-31G(d) level.[68] We only take HOMO into consideration when evaluating transfer integral since the energy difference between HOMO and HOMO-1 is large enough (0.6~0.8 eV) for the molecules considered here. The neighbor list was established for every molecular pair having a distance between their nearest fragments within 7 Å. After all parameters defined for each hopping site and each molecular pair appear in **Equation 1** were computed, kinetic Monte Carlo (kMC) simulation was performed with 10 ms simulation time and a 10^5 Vcm^{-1} electric field. The hole mobility was determined from an average charge velocity.[60] For each molecule, 100 snapshots of an MD trajectory were taken for kMC simulations to reach better statistics. For a given MD snapshot, KMC simulations with electric field of six different directions (x, y, z, -x, -y, and -z) were conducted resulting in 600 kMC simulations for each molecule.

Molecular transport network

The connectivity of the molecular transport network was investigated based on a graph constructed for each molecule, where the vertices are the molecular centers of mass and the edges are the square of transfer integrals equal to or higher than a certain threshold value (see SI).[69] The connectivity is evaluated by examining the histogram of the number of edges (connections) of each hopping site. The average number of edges per hopping site serves as a quantitative descriptor for the connectivity of the molecular network. The threshold values of J^2 are from 10^{-6} to 10^{-4} eV^2. For a threshold above 10^{-4} eV^2, almost all hopping sites possess 0 edge. Yet, J^2 values smaller than 10^{-6} eV^2 have a negligible contribution to the effective hole transport. The histograms for the different MD snapshots are very similar and the results shown here are thus from one MD snapshot and the total counts of a histogram sum to 512 (total number of molecules in a simulation box). For more information, please see the supporting information.

Clustering of dimer configurations

The dimer configurations of an HTM were clustered through defining a cartesian coordinate system, where each dimer configuration can be represented as a point with coordinates. The k-means clustering algorithm, which is a reasonable choice for our task,[70] was used in junction with the elbow method to find the optimal number of clusters (**Figure S10**). For more information, please see the supporting information.

Ionization potential

The ionization potentials of the solid-state amorphous HTMs were computed using a computational protocol proposed by Andrienko et. al.,[28] which has shown a good agreement between computed and experimental IPs. Correction terms based on the Thole model were added to the isolated gas phase IP to account for the solid state effect (electrostatic and induction effect from surrounding molecules). The isolated gas phase IP was computed using the ΔSCF procedure in conjunction with B3LYP functional and the 6-31G(d,p) basis set.

$$IP_{\mathrm{solid}} = IP_{\mathrm{iso}} + E_{\mathrm{corr}} - 2\sigma \quad (7)$$

$$IP_{\mathrm{iso}} = \Delta SCF = E_{\mathrm{cN}} - E_{\mathrm{nN}} \quad (8)$$

where $IP_{\mathrm{solid}}/IP_{\mathrm{iso}}$ is the ionization potential of an HTM in solid state/isolated gas phase, E_{corr} is the IP correction term from electrostatic and induction effect, σ is the standard deviation of the site energy distribution, and $E_{\mathrm{nN}}/E_{\mathrm{cN}}$ is the total energy of the neutral/cationic molecule in a neutral geometry.

4.2 Experimental Details

Hole mobility measurement

The hole mobility of TPA3C3M and TPA3C3PD was measured by field effect transistors with a bottom gate bottom contact (BGBC) configuration. The BGBC transistor substrates are purchased from Fraunhofer Institute for Photonic Microsystems. N-doped silicon wafer and a SiO_2 layer (230 nm) are utilized as bottom gate electrode and dielectric layer, respectively. A 30 nm Au is applied as source and drain electrodes, and a 10 nm ITO layer is used to improve the adhesion of Au on SiO_2. The channel length (L) and width (W) of the BGBC transistor substrate are 2.5 μm and 10 mm, respectively. The substrate was washed by water, acetone and isopropanol before use. TPA3C3M and TPA3C3PD were dissolved in chloroform with a concentration of 5 mg mL^{-1}. A 50 nm thin film of TPA3C3M or TPA3C3PD was deposited on the transistor substrate by spin coating the solution at 1000 rpm. After spin-coating, the substrates were annealed at 100 °C. The current-voltage (I-V) characteristics of the transistors were measured in nitrogen glovebox using a custom-built probe station and a Keithley 2612A dual-channel source measure unit. The electron mobility of the transistors was extracted from saturation regime according to the equation:

$$\mu = 2\left(\frac{\partial\sqrt{I_{D,sat}}}{\partial V_{GS}}\right)^2 \frac{L}{WC_i} \quad (9)$$

where L and W are the channel length and width, respectively. $I_{D,sat}$ is the current between source and drain electrode at saturation, and V_{GS} is the gate-source voltage. C_i (1.4×10^{-8} F cm^{-2}) is the capacity of the dielectric layer.

Synthesis of HTMs

The general synthetic information of TPA3C3M and TPA3C3PD molecules can be found in supporting information.

ASSOCIATED CONTENT

Supporting Information

Computational information including electronic properties, transport properties and analysis (reorganization energy, electronic coupling, molecular dipole moment distribution and dimer configuration clustering). Experimental information including general synthetic information and hole mobility measurement of HTMs.

AUTHOR INFORMATION

Corresponding Author

*E-mail: clemence.corminboeuf@epfl.ch.

ORCID

Clémence Corminboeuf: 0000-0001-7993-2879

Kevin Sivula: 0000-0002-8458-0270

Author Contributions

The manuscript was written through contributions of all authors. All authors have given approval to the final version of the manuscript.

Notes

The authors declare no competing financial interest.

ACKNOWLEDGMENT

C.C. and K.H.L. thank the European Research Council (ERC starting Grant 306528, COMPOREL) for financial support. M.K.N. acknowledges funding by the Qatar Environment and Energy Research Institute (QEERI), Hamad Bin Khalifa University (HBKU), Qatar Foundation Doha, Qatar.

REFERENCES

(1) Saliba, M.; Correa-Baena, J.-P.; Grätzel, M.; Hagfeldt, A.; Abate, A. Perovskite Solar Cells: From the Atomic Level to Film Quality and Device Performance. *Angew. Chemie Int. Ed.* **2018**, *57* (10), 2554–2569.

(2) Miyasaka, T.; Kojima, A.; Teshima, K.; Shirai, Y. Organometal Halide Perovskites as Visible-Light Sensitizers for Photovoltaic Cells. *J. Am. Chem. Soc.* **2009**, *131* (17), 6050–6051.

(3) Liu, X.; Zhu, L.; Zhang, F.; You, J.; Xiao, Y.; Li, D.; Wang, S.; Meng, Q.; Li, X. Stable Perovskite Solar Cells Based on Hydrophobic Triphenylamine Hole-Transport Materials. *Energy Technol.* **2017**, *5* (2), 312–320.

(4) Zheng, L.; Chung, Y. H.; Ma, Y.; Zhang, L.; Xiao, L.; Chen, Z.; Wang, S.; Qu, B.; Gong, Q. A Hydrophobic Hole Transporting Oligothiophene for Planar Perovskite Solar Cells with Improved Stability. *Chem. Commun.* **2014**, *50* (76), 11196–11199.

(5) Rodríguez-Seco, C.; Cabau, L.; Vidal-Ferran, A.; Palomares, E. Advances in the Synthesis of Small Molecules as Hole Transport Materials for Lead Halide Perovskite Solar Cells. *Acc. Chem. Res.* **2018**, *51* (4), 869–880.

(6) Agarwala, P.; Kabra, D. A Review on Triphenylamine (TPA) Based Organic Hole Transport Materials (HTMs) for Dye Sensitized Solar Cells (DSSCs) and Perovskite Solar Cells (PSCs): Evolution and Molecular Engineering. *J. Mater. Chem. A* **2017**, *5* (4), 1348–1373.

(7) Zhang, F.; Wang, S.; Zhu, H.; Liu, X.; Liu, H.; Li, X.; Xiao, Y.; Zakeeruddin, S. M.; Grätzel, M. Impact of Peripheral Groups on Phenothiazine-Based Hole-Transporting Materials for Perovskite Solar Cells. *ACS Energy Lett.* **2018**, *3* (5), 1145–1152.

(8) García-Benito, I.; Zimmermann, I.; Urieta-Mora, J.; Aragó, J.; Calbo, J.; Perles, J.; Serrano, A.; Molina-Ontoria, A.; Ortí, E.; Martín, N.; Nazeeruddin, M. K. Heteroatom Effect on Star-Shaped Hole-Transporting Materials for Perovskite Solar Cells. *Adv. Funct. Mater.* **2018**, *28* (31), 1–10.

(9) Xiang, F.-X.; Wang, X.-L.; Dou, S.-X. Molecular Engineering of Copper Phthalocyanines: A Strategy in Developing Dopant- Free Hole-Transporting Materials for Efficient and Ambient-Stable Perovskite Solar Cells. *Adv. Energy Mater.* **2018**, *1803287*, 11.

(10) Magomedov, A.; Paek, S.; Gratia, P.; Kasparavicius, E.; Daskeviciene, M.; Kamarauskas, E.; Gruodis, A.; Jankauskas, V.; Kantminiene, K.; Cho, K. T.; Rakstys, K.; Malinauskas, T.; Getautis, V.; Nazeeruddin, M. K. Diphenylamine-Substituted Carbazole-Based Hole Transporting Materials for Perovskite Solar Cells: Influence of Isomeric Derivatives. *Adv. Funct. Mater.* **2018**, *28* (9), 1–13.

(11) Petrus, M. L.; Schutt, K.; Sirtl, M. T.; Hutter, E. M.; Closs, A. C.; Ball, J. M.; Bijleveld, J. C.; Petrozza, A.; Bein, T.; Dingemans, T. J.; Savenije, T. J.; Snaith, H.; Docampo, P. New Generation Hole Transporting Materials for Perovskite Solar Cells: Amide-Based Small-Molecules with Nonconjugated Backbones. *Adv. Energy Mater.* **2018**, *8* (32), 1–11.

(12) Pham, H. D.; Do, T. T.; Kim, J.; Charbonneau, C.; Manzhos, S.; Feron, K.; Tsoi, W. C.; Durrant, J. R.; Jain, S. M.; Sonar, P. Molecular Engineering Using an Anthanthrone Dye for Low-Cost Hole Transport Materials: A Strategy for Dopant-Free, High-Efficiency, and Stable Perovskite Solar Cells. *Adv. Energy Mater.* **2018**, *8* (16), 1–13.

(13) Zhang, J.; Xu, B.; Yang, L.; Ruan, C.; Wang, L.; Liu, P.; Zhang, W.; Vlachopoulos, N.; Kloo, L.; Boschloo, G.; Sun, L.; Hagfeldt, A.; Johansson, E. M. J. The Importance of Pendant Groups on Triphenylamine-Based Hole Transport Materials for Obtaining Perovskite Solar Cells with over 20% Efficiency. *Adv. Energy Mater.* **2018**, *8* (2), 1–12.

(14) Alberga, D.; Mangiatordi, G. F.; Labat, F.; Ciofini, I.; Nicolotti, O.; Lattanzi, G.; Adamo, C. Theoretical Investigation of Hole Transporter Materials for Energy Devices. *J. Phys. Chem. C* **2015**, *119* (42), 23890–23898.

(15) Lin, K. H.; Prlj, A.; Corminboeuf, C. A Rising Star: Truxene as a Promising Hole Transport Material in Perovskite Solar Cells. *J. Phys. Chem. C* **2017**, *121* (39), 21729–21739.

(16) Urieta-Mora, J.; García-Benito, I.; Molina-Ontoria, A.; Martín, N. Hole Transporting Materials for Perovskite Solar Cells: A Chemical Approach. *Chem. Soc. Rev.* **2018**, *47* (23).

(17) Lin, K.-H.; Prlj, A.; Corminboeuf, C. How Does Alkyl Chain Length Modify the Properties of Triphenylamine-Based Hole Transport Materials? *J. Mater. Chem. C* **2018**, *6* (5), 960–965.

(18) Chi, W.-J.; Zheng, D.-Y.; Chen, X.-F.; Li, Z.-S. Optimizing Thienothiophene Chain Lengths of D–π–D Hole Transport Materials in Perovskite Solar Cells for Improving Energy Levels and Hole Mobility. *J. Mater. Chem. C* **2017**, *5*, 10055–10060.

(19) Sandoval-Torrientes, R.; Zimmermann, I.; Calbo, J.; Aragó, J.; Santos, J.; Ortí, E.; Martín, N.; Nazeeruddin, M. K. Hole Transporting Materials Based on Benzodithiophene and Dithienopyrrole Cores for Efficient Perovskite Solar Cells. *J. Mater. Chem. A* **2018**, *6* (14), 5944–5951.

(20) Wang, J.; Wang, S.; Li, X.; Zhu, L.; Meng, Q.; Xiao, Y.; Li, D. Novel Hole Transporting Materials with a Linear π-Conjugated Structure for Highly Efficient Perovskite Solar Cells. *Chem. Commun.* **2014**, *50* (44), 5829–5832.

(21) Wu, Y.; Wang, Z.; Liang, M.; Cheng, H.; Li, M.; Liu, L.; Wang, B.; Wu, J.; Prasad Ghimire, R.; Wang, X.; Sun, Z.; Xue, S.; Qiao, Q. Influence of Nonfused Cores on the Photovoltaic Performance of Linear Triphenylamine-Based Hole-Transporting Materials for Perovskite Solar Cells. *ACS Appl. Mater. Interfaces* **2018**, *10* (21), 17883–17895.

(22) Liu, X.; Kong, F.; Jin, S.; Chen, W.; Yu, T.; Hayat, T.; Alsaedi, A.; Wang, H.; Tan, Z.; Chen, J.; Dai, S. Molecular Engineering of Simple Benzene-Arylamine Hole-Transporting Materials for Perovskite Solar Cells. *ACS Appl. Mater. Interfaces* **2017**, *9* (33), 27657–27663.

(23) Li, M.; Wang, Z.; Liang, M.; Liu, L.; Wang, X.; Sun, Z.; Xue, S. Low-Cost Carbazole-Based Hole-Transporting Materials for Perovskite Solar Cells: Influence of S,N-Heterocycle. *J. Phys. Chem. C* **2018**, *122* (42), 24014–24024.

(24) Liu, X.; Kong, F.; Chen, W.; Yu, T.; Huang, Y.; Hayat, T.; Alsaedi, A.; Wang, H.; Chen, J.; Dai, S. Improving the Performance of Arylamine-Based Hole Transporting Materials in Perovskite Solar Cells: Extending π-Conjugation Length or Increasing the Number of Side Groups? *J. Energy Chem.* **2018**, *27* (5), 1409–1414.

(25) Jeon, N. J.; Lee, H. G.; Kim, Y. C.; Seo, J.; Noh, J. H.; Lee, J.; Seok, S. Il. O-Methoxy Substituents in Spiro-OMeTAD for Efficient Inorganic-Organic Hybrid Perovskite Solar Cells. *J. Am. Chem. Soc.* **2014**, *136* (22), 7837–7840.

(26) Zimmermann, I.; Urieta-Mora, J.; Gratia, P.; Aragï¿½, J.; Grancini, G.; Molina-Ontoria, A.; Ortï¿½, E.; Martï¿½n, N.; Nazeeruddin, M. K. High-Efficiency Perovskite Solar Cells Using Molecularly Engineered, Thiophene-Rich, Hole-Transporting Materials: Influence of Alkyl Chain Length on Power Conversion Efficiency. *Adv. Energy Mater.* **2017**, *7* (6), 1–8.

(27) Gryn'ova, G.; Lin, K.-H.; Corminboeuf, C. Read between the Molecules: Computational Insights into Organic Semiconductors. *J. Am. Chem. Soc.* **2018**, *140* (48), 16370–16386.

(28) Kotadiya, N. B.; Mondal, A.; Xiong, S.; Blom, P. W. M.; Andrienko, D.; Wetzelaer, G. J. A. H. Rigorous Characterization and Predictive Modeling of Hole Transport in Amorphous

Organic Semiconductors. *Adv. Electron. Mater.* **2018**, *1800366*, 1–7.

(29) Park, S. J.; Jeon, S.; Lee, I. K.; Zhang, J.; Jeong, H.; Park, J.-Y.; Bang, J.; Ahn, T. K.; Shin, H.-W.; Kim, B.-G.; Park, H. J. Inverted Planar Perovskite Solar Cells with Dopant Free Hole Transporting Material: Lewis Base-Assisted Passivation and Reduced Charge Recombination. *J. Mater. Chem. A* **2017**, *5* (25), 13220–13227.

(30) Marcus, R. a. Electron Transfer Reactions in Chemistry: Theory and Experiment. *Angew. Chemie Int. Ed. English* **1993**, *32* (8), 1111–1121.

(31) Urieta-Mora, J.; Zimmermann, I.; Aragó, J.; Molina-Ontoria, A.; Ortí, E.; Martín, N.; Nazeeruddin, M. K. Dibenzoquinquethiophene- and Dibenzosexithiophene-Based Hole-Transporting Materials for Perovskite Solar Cells. *Chem. Mater.* **2018**, acs.chemmater.8b04003.

(32) Kou, C.; Feng, S.; Li, H.; Li, W.; Li, D.; Meng, Q.; Bo, Z. Molecular "Flower" as the High-Mobility Hole-Transport Material for Perovskite Solar Cells. *ACS Appl. Mater. Interfaces* **2017**, *9* (50), 43855–43860.

(33) Atahan-Evrenk, Ş.; Aspuru-Guzik, A. Prediction and Theoretical Characterization of P-Type Organic Semiconductor Crystals for Field-Effect Transistor Applications. In *Journal of Arthropod-Borne Diseases*; 2014; Vol. 12, pp 95–138.

(34) Watanabe, M.; Chang, Y. J.; Liu, S. W.; Chao, T. H.; Goto, K.; Islam, M. M.; Yuan, C. H.; Tao, Y. T.; Shinmyozu, T.; Chow, T. J. The Synthesis, Crystal Structure and Charge-Transport Properties of Hexacene. *Nat. Chem.* **2012**, *4* (7), 574–578.

(35) Coropceanu, V.; Cornil, J.; da Silva Filho, D. A.; Olivier, Y.; Silbey, R.; Brédas, J. L. Charge Transport in Organic Semiconductors. *Chem. Rev.* **2007**, *107* (4), 926–952.

(36) Bässler, H. Charge Organic Photoconductors a Monte Carlo Simulation Study. *Phys. Status Solidi B* **1993**, *175*, 15–56.

(37) Coehoorn, R.; Pasveer, W. F.; Bobbert, P. A.; Michels, M. A. J. Charge-Carrier Concentration Dependence of the Hopping Mobility in Organic Materials with Gaussian Disorder. *Phys. Rev. B - Condens. Matter Mater. Phys.* **2005**, *72* (15), 1–20.

(38) Friederich, P.; Meded, V.; Poschlad, A.; Neumann, T.; Rodin, V.; Stehr, V.; Symalla, F.; Danilov, D.; Lüdemann, G.; Fink, R. F.; Kondov, I.; von Wrochem, F.; Wenzel, W. Molecular Origin of the Charge Carrier Mobility in Small Molecule Organic Semiconductors. *Adv. Funct. Mater.* **2016**, *26* (31), 5757–5763.

(39) Nikitenko, V. R.; Sukharev, V. M. Transport Level in Disordered Organics: Correlated Energetic Disorder in Dipole Glass Model. *J. Phys. Conf. Ser.* **2016**, *741* (1), 1–5.

(40) Schrader, M.; Körner, C.; Elschner, C.; Andrienko, D. Charge Transport in Amorphous and Smectic Mesophases of Dicyanovinyl-Substituted Oligothiophenes. *J. Mater. Chem.* **2012**, *22* (41), 22258–22264.

(41) Vehoff, T.; Baumeier, B.; Troisi, A.; Andrienko, D. Charge Transport in Organic Crystals: Role of Disorder and Topological Connectivity. *J. Am. Chem. Soc.* **2010**, *132* (33), 11702–11708.

(42) Jackson, N. E.; Savoie, B. M.; Chen, L. X.; Ratner, M. A. A Simple Index for Characterizing Charge Transport in Molecular Materials. *J. Phys. Chem. Lett.* **2015**, *6* (6), 1018–1021.

(43) Hu, Z.; Fu, W.; Yan, L.; Miao, J.; Yu, H.; He, Y.; Goto, O.; Meng, H.; Chen, H.; Huang, W. Effects of Heteroatom Substitution in Spiro-Bifluorene Hole Transport Materials. *Chem. Sci.* **2016**, *7* (8), 5007–5012.

(44) Wu, F.; Shan, Y.; Qiao, J.; Zhong, C.; Wang, R.; Song, Q.; Zhu, L. Replacement of Biphenyl by Bipyridine Enabling Powerful Hole Transport Materials for Efficient Perovskite Solar Cells. *ChemSusChem* **2017**, *10* (19), 3833–3838.

(45) Rakstys, K.; Paek, S.; Gao, P.; Gratia, P.; Marszalek, T.; Grancini, G.; Cho, K. T.; Genevicius, K.; Jankauskas, V.; Pisula, W.; Nazeeruddin, M. K. Molecular Engineering of Face-on Oriented Dopant-Free Hole Transporting Material for Perovskite Solar Cells with 19% PCE. *J. Mater. Chem. A* **2017**, *5* (17), 7811–7815.

(46) Steck, C.; Franckevičius, M.; Zakeeruddin, S. M.; Mishra, A.; Bäuerle, P.; Grätzel, M. A-D-A-Type S,N-Heteropentacene-Based Hole Transport Materials for Dopant-Free Perovskite Solar Cells. *J. Mater. Chem. A* **2015**, *3* (34), 17738–17746.

(47) Van Der Spoel, D.; Lindahl, E.; Hess, B.; Groenhof, G.; Mark, A. E.; Berendsen, H. J. C. GROMACS: Fast, Flexible, and Free. *J. Comput. Chem.* **2005**, *26* (16), 1701–1718.

(48) Berendsen, H. J. C.; van der Spoel, D.; van Drunen, R. GROMACS: A Message-Passing Parallel Molecular Dynamics Implementation. *Comput. Phys. Commun.* **1995**, *91* (1–3), 43–56.

(49) Abraham, M. J.; Murtola, T.; Schulz, R.; Páll, S.; Smith, J. C.; Hess, B.; Lindahl, E. GROMACS: High Performance Molecular Simulations through Multi-Level Parallelism from Laptops to Supercomputers. *SoftwareX* **2015**, *1–2*, 19–25.

(50) Vanommeslaeghe, K.; Hatcher, E.; Acharya, C.; Kundu, S.; Zhong, S.; Shim, J.; Darian, E.; Guvench, O.; Lopes, P.; Vorobyov, I.; Mackerell, A. D. CHARMM General Force Field: A Force Field for Drug-like Molecules Compatible with the CHARMM All-Atom Additive Biological Force Fields. *J. Comput. Chem.* **2009**, *31* (16), NA-NA.

(51) Yu, W.; He, X.; Vanommeslaeghe, K.; MacKerell, A. D. Extension of the CHARMM General Force Field to Sulfonyl-Containing Compounds and Its Utility in Biomolecular Simulations. *J. Comput. Chem.* **2012**, *33* (31), 2451–2468.

(52) Bayly, C. I.; Cieplak, P.; Cornell, W.; Kollman, P. a. A Well-Behaved Electrostatic Potential Based Method Using Charge Restraints for Deriving Atomic Charges: The RESP Model. *J. Phys. Chem.* **1993**, *97* (40), 10269–10280.

(53) Bussi, G.; Donadio, D.; Parrinello, M. Canonical Sampling through Velocity Rescaling. *J. Chem. Phys.* **2007**, *126* (1).

(54) Ma, H.; Liu, N.; Huang, J.-D. A DFT Study on the Electronic Structures and Conducting Properties of Rubrene and Its Derivatives in Organic Field-Effect Transistors. *Sci. Rep.* **2017**, *7* (1), 331.

(55) Geng, H.; Niu, Y.; Peng, Q.; Shuai, Z.; Coropceanu, V.; Brédas, J. L. Theoretical Study of Substitution Effects on Molecular Reorganization Energy in Organic Semiconductors. *J. Chem. Phys.* **2011**, *135* (10).

(56) Stephens, P. J.; Devlin, F. J.; Chabalowski, C. F.; Frisch, M. J. Ab Initio Calculation of Vibrational Absorption and Circular Dichroism Spectra Using Density Functional Force Fields. *J. Phys. Chem.* **1994**, *98* (45), 11623–11627.

(57) Becke, A. D. Density-functional Thermochemistry. III. The Role of Exact Exchange. *J. Chem. Phys.* **1993**, *98* (7), 5648–5652.

(58) Grimme, S.; Ehrlich, S.; Goerigk, L. Effect of the Damping Function in Dispersion Corrected Density Functional Theory. *J. Comput. Chem.* **2011**, *32* (7), 1456–1465.

(59) Frisch, M. J.; Trucks, G. W.; Schlegel, H. B.; Scuseria, G. E.; Robb, M. A.; Cheeseman, J. R.; Scalmani, G.; Barone, V.; Petersson, G. A.; Nakatsuji, H.; Li, X.; Caricato, M.; Marenich, A. V.; Bloino, J.; Janesko, B. G.; Gomperts, R.; Mennucci, B.; Hratchian, H. P.; J. V. Ortiz; Izmaylov, A. F.; Sonnenberg, J. L.; Williams-Young, D.; Ding, F.; Lipparini, F.; Egidi, F.; Goings, J.; Peng, B.; Petrone, A.; Henderson, T.; Ranasinghe, D.; Zakrzewski, V. G.; Gao, J.; Rega, N.; Zheng, G.; Liang, W.; Hada, M.; Ehara, M.; Toyota, K.; Fukuda, R.; Hasegawa, J.; Ishida, M.; Nakajima, T.; Honda, Y.; Kitao, O.; Nakai, H.; Vreven, T.; Throssell, K.; Montgomery, J. A.; Jr., J. E. P.; Ogliaro, F.; Bearpark, M. J.; Heyd, J. J.; Brothers, E. N.; Kudin, K. N.; Staroverov, V. N.; Keith, T. A.; Kobayashi, R.; Normand, J.; Raghavachari, K.; Rendell, A. P.; Burant, J. C.; Iyengar, S. S.; Tomasi, J.; Cossi, M.; Millam, J. M.; Klene, M.; Adamo, C.; Cammi, R.; Ochterski, J. W.; Martin, R. L.; Morokuma, K.; Farkas, O.; Foresman, J. B.; Fox, D. J. Gaussian 16, Revision B.01. **2016**, Gaussian, Inc., Wallingford CT.

(60) Victor, R.; Lukyanov, A.; May, F.; Schrader, M.; Veho, T.; Kirkpatrick, J.; Andrienko, D.; Rühle, V.; Lukyanov, A.; May, F.; Schrader, M.; Vehoff, T.; Kirkpatrick, J.; Baumeier, B.; Andrienko, D.; Victor, R.; Lukyanov, A.; May, F.; Schrader, M.; Veho, T.; Kirkpatrick, J.; Andrienko, D. Microscopic Simulations of Charge Transport in Disordered Organic Semiconductors. *J. Chem. Theory Comput.* **2011**, *7*, 3335–3345.

(61) Rühle, V.; Lukyanov, A.; May, F.; Schrader, M.; Vehoff, T.; Kirkpatrick, J.; Baumeier, B.; Andrienko, D. Microscopic Simulations of Charge Transport in Disordered Organic Semiconductors. *J. Chem. Theory Comput.* **2011**, *7* (10), 3335–3345.

(62) D'Avino, G.; Muccioli, L.; Castet, F.; Poelking, C.; Andrienko, D.; Soos, Z. G.; Cornil, J.; Beljonne, D. Electrostatic Phenomena in Organic Semiconductors: Fundamentals and Implications for Photovoltaics. *J. Phys. Condens. Matter* **2016**, *28* (43).

(63) Thole, B. T. Molecular Polarizabilities Calculated with a Modified Dipole Interaction. *Chem. Phys.* **1981**, *59* (3), 341–350.
(64) Carey, C.; Chirlian, L. E.; Francl, M. M.; Gange, D. M. Beyond CHELP: Improved Potential Derived Charges for Sugars. *Glycoconj. J.* **1997**, *14* (4), 501–505.
(65) Lin, J. B.; Darzi, E. R.; Jasti, R.; Yavuz, I.; Houk, K. N. Solid-State Order and Charge Mobility in [5]- to [12]Cycloparaphenylenes. *J. Am. Chem. Soc.* **2019**, *141* (2), 952–960.
(66) Baumeier, B.; Kirkpatrick, J.; Andrienko, D. Density-Functional Based Determination of Intermolecular Charge Transfer Properties for Large-Scale Morphologies. *Phys. Chem. Chem. Phys.* **2010**, *12* (36), 11103–11113.
(67) Kirkpatrick, J. An Approximate Method for Calculating Transfer Integrals Based on the ZINDO Hamiltonian. *Int. J. Quantum Chem.* **2008**, *108* (1), 51–56.
(68) Yavuz, I.; Lin, J. B.; Houk, K. N. Impact of Morphology, Side-Chains, and Crystallinity on Charge-Transport Properties of π-Extended Double Helicenes. *Phys. Chem. Chem. Phys.* **2019**, *21* (2), 901–914.
(69) Savoie, B. M.; Kohlstedt, K. L.; Jackson, N. E.; Chen, L. X.; Olvera de la Cruz, M.; Schatz, G. C.; Marks, T. J.; Ratner, M. A. Mesoscale Molecular Network Formation in Amorphous Organic Materials. *Proc. Natl. Acad. Sci.* **2014**, *111* (28), 10055–10060.
(70) Jain, A. K. Data Clustering: 50 Years beyond K-Means. *Pattern Recognit. Lett.* **2010**, *31* (8), 651–666.

Insert Table of Contents artwork here